# Modeling the High Mercury Wet deposition in the Southeastern US by WRF-GC-Hg v1.0

Xiaotian Xu[1, a], Xu Feng[2, b], Haipeng Lin[3], Peng Zhang[1], Shaojian Huang[1], Zhengcheng Song[1], Yiming Peng[1], Tzung-May Fu[4], Yanxu Zhang*[1]

[1] Department of Atmospheric Sciences, Nanjing University, Nanjing, Jiangsu, China
[2] Department of Atmospheric and Oceanic Sciences, School of Physics, Peking University, Beijing, China
[3] John A. Paulson School of Engineering and Applied Sciences, Harvard University, Cambridge, Massachusetts, USA
[4] School of Environmental Science and Engineering, Southern University of Science and Technology, Shenzhen, Guangdong, China
[a] Current affiliation: Department of Atmospheric Science, University of Illinois at Urbana-Champaign, Urbana, IL, USA
[b] Current affiliation: John A. Paulson School of Engineering and Applied Sciences, Harvard University, Cambridge, Massachusetts, USA

**Correspondence**: Yanxu Zhang (zhangyx@nju.edu.cn)

**Abstract.** High mercury wet deposition in the southeastern United States has been noticed for many years. Previous studies came up with a theory that it was associated with high-altitude divalent mercury scavenged by convective precipitation. Given the coarse resolution of previous models (e.g. GEOS-Chem), this theory is still not fully tested. Here we employed a newly developed WRF-GEOS-Chem (WRF-GC) model implemented with mercury simulation (WRF-GC-Hg v1.0). We conduct extensive model benchmarking by comparing WRF-GC with different resolutions (from 50 km to 25 km) to GEOS-Chem output ($4° \times 5°$) and data from Mercury Deposition Network (MDN) in July-September 2013. The comparison of mercury wet deposition from two models both presents high mercury wet deposition in the southeastern United States. We divided simulation results by heights (2km, 4km, 6km, 8km), different types of precipitation (large-scale and convective), and combinations of these two variations together and find most mercury wet deposition concentrates on higher level and is caused by convective precipitation. Therefore, we conclude that it is the deep convection that caused enhanced mercury wet deposition in the southeastern United States.

## 1 Introduction

Mercury (Hg) is one of the most toxic heavy metals in our environment. Atmospheric Hg can undergo long-range transport (Ariya et al., 2015) in three major forms: gaseous elemental mercury (GEM), gaseous oxidized mercury (GOM), and particle-bound mercury (PBM). GEM has extremely low water solubility with a relatively long (~0.5-1 year) residence time in the atmosphere. GEM is slowly oxidized to GOM in the atmosphere initialized by bromine atoms (Holmes et al.,

2010), especially in the high-altitudes due to low temperature (Lyman and Jaffe, 2012). While GOM has a much shorter atmospheric lifetime than GEM due to its strong water solubility and subsequent removal by precipitation (Gonzalez-Raymat et al., 2017; Kaulfus et al., 2017), PBM has a similar residence time with GOM due to dry and wet deposition near the source regions (Sexauer Gustin et al., 2012; Coburn et al., 2016).

Wet deposition is a major process for Hg to enter the aquatic and terrestrial ecosystems, wherein causing significant ecological and human health risks (Selin et al., 2007; Rumbold et al., 2019; Fu et al., 2016). The wet deposition flux is thus extensively measured globally, especially in the United States by the Hg Deposition Network (MDN), which was started in 1996 and expanded to contain 81active sites and 117 inactive sites at the present day (Prestbo and Gay, 2009). Previous studies have reported spatial and temporal variation of wet deposition of Hg from over 100 sites spanning from1996 to 2005 and found that Hg wet deposition was high in summer and low in winter and have a distribution that Southeast > Ohio River > Midwest > Northeast. The continuous high-level concentration together with a large amount of precipitation every year results in high Hg wet deposition in the southeastern region, especially from the Gulf of Mexico to Florida. This level of Hg wet deposition can extend northward to Mississippi Valley. The Hg wet deposition in the Midwestern region was relatively moderate and was lowest in northeastern because the precipitation was lower in these areas. Other studies also found out that the Hg wet deposition flux had strong seasonality with a maximum in summer, which was especially true for Florida with approximately 80% of rainfall amount and Hg wet deposition happening during it (Mason et al., 2000; Fulkerson and Nnadi, 2006; Kaulfus et al., 2017).

One unique phenomenon observed by the MDN sites is the maximum deposition flux over the southeast US, contradicting with that of $NO_3^-$ and $SO_4^{2-}$ that is the maximum over northeast US (http://http://nadp.slh.wisc.edu/data/annualmaps.aspx). The high deposition over this region is hypothesized to be caused by the scavenging of high-concentration GOM in the free troposphere by convective precipitation (Guentzel et al., 2001; Selin et al., 2008). This hypothesis is partially confirmed by Holmes et al., 2016, which found the rain Hg concentrations in seven sites are increased by 50% by thunderstorms relative to weak convective or stratiform events of equal precipitation depth. Kaulfus et al., 2017 found similar patterns for more MDN sites operated in 2005-2013. However, numerical models have trouble reproducing this unique spatial pattern (Holmes et al., 2010), since the global model is generally too coarse to capture deep convective cells that have much smaller spatial scales (Brisson et al., 2016). Later, Zhang et al., 2016 developed a nested-grid simulation of Hg over North America with a higher resolution (1/2° latitude × 2/3° longitude), which improves the model results but still with a significantly low bias in this region, leaving an unclosed budget. Except for GEOS-Chem (Zhang et al., 2012), Hg simulation was implemented into many models like WRF-Chem (Gencarelli et al., 2014), CMAQ (Bullock and Brehme, 2002) and STEM-Hg (Pan et al., 2010), etc. Models like WRF-Chem and CMAQ also use WRF for meteorology simulation, with different Hg chemistry libraries that have not been updated in recent years. Therefore, we chose WRF-GC (Feng et al., 2021; Lin et al., 2020) to develop a new Hg simulation capacity with a complimentary Hg library because WRF-GC has several advantages: 1) It has flexible resolution and widely accepted meteorology simulation

provided by WRF model; 2) The Hg chemistry included by GEOS-Chem model is more up-to-date than many other models (Horowitz et al., 2017); 3) It is relatively easy to port Hg library from GEOS-Chem to WRF-GC-Hg. We will further test if the higher (deep) convective precipitation over the southeast US can fully explain the elevated Hg wet deposition fluxes in this region.

## 2 Materials and methods

### 1.1 WRF-GC model with Hg

We develop a new simulation capacity (WRF-GC-Hg v1.0) for atmospheric Hg emission, transport, chemistry, and deposition based on the WRF-GC v1.0, which is fully described by Lin et al., 2020 and Feng et al., 2021 (For short, keep using WRF-GC for WRF-GC-Hg v1.0 in the following paragraphs). The model's framework is shown in Fig. 1. Briefly, the model contains three parts: the Weather Research Forecasting (WRF) mesoscale meteorological model (https://www.mmm.ucar.edu/weather-research-and-forecasting-model), the GEOS-Chem global 3-D atmospheric chemistry model (http://acmg.seas.harvard.edu/geos/) and the WRF-GC coupler. The WRF v3.9.1.1 (https://github.com/wrf-model/WRF/tree/V3.9.1.1)-Advanced Research WRF (ARW) solver is used to simulate meteorological processes and the advection of the compositions of the atmosphere with GEOS-Chem v12.2.1 (https://doi.org/10.5281/zenodo.2580198) as a self-contained chemical module. The WRF-GC coupler consists of an interface, state conversion, and management module for the two parent models. On one hand, the WRF-GC model can take advantage of the WRF model to simulate meteorology in highly customized model domains and resolutions. In addition, the WRF offers options for configuration, vertical levels, horizontal grids, and map projections. The WRF also supplies options for land surface physics, planetary boundary layer physics, radiative transfer, cloud microphysics, and cumulus parameterization (Skamarock et al., 2008). On the other hand, the WRF-GC inherits the state-of-the-art emission, chemistry, and deposition simulation from the GEOS-Chem model.(Eastham et al., 2018; Long et al., 2015) All chemical configurations, including chemical species, mechanisms, emissions, and diagnostics can be customized using *FlexChem* pre-processor, a wrapper for the Kinetic-Pre-Processor (KPP) that allows users to add chemical species and reactions and develop their chemical mechanism (Damian et al., 2002; Sandu and Sander, 2006). The standard chemistry option of GEOS-Chem includes a full Ox-NOx-VOC-halogen-aerosol chemistry mechanism for the troposphere that contains 208 chemical species and 981 reactions and a unified tropospheric-stratospheric chemistry extension (UCX) (Eastham et al., 2014).

We implement a complimentary Hg chemistry library (see Fig. 1) to the WRF-GC model by first introducing Hg species in the GEOS-Chem module: $Hg^0$ (GEM), $Hg^2$ (GOM), HgP (PBM), and two Hg(I) species (HgBr and HgCl). The chemical reactions of Hg involve the two-stage oxidation of $Hg^0$ to Hg(I) and $Hg^2$ by halogens, and the reaction rates are following Horowitz et al., 2017. Similarly, the aqueous phase reduction of GOM to $Hg^0$ in cloud droplets, and the partitioning of $Hg^2$ and HgP on aerosols are also included. These Hg species and reactions are added to the standard GEOS-

Chem KPP solver so the concentrations of chemicals that can react with Hg (e.g., Br, BrO, OH, $NO_2$) can be directly read online. Similar to other species in GEOS-Chem, the emissions of Hg are handled by the Harmonized Emission Component (HEMCO) (Lin et al., 2021). We use the WHET emission inventory ($1° \times 1°$) for the anthropogenic Hg emissions (Zhang et

100   al., 2016) as well as natural emission and re-emissions inventory ($4° \times 5°$) from (Horowitz et al., 2017) (see Fig. 1). The re-emissions from soil, snow, and ocean are not dynamically modeled but directly read in as a static monthly emission inventory through HEMCO based on a former GEOS-Chem Hg simulation (Horowitz et al., 2017).
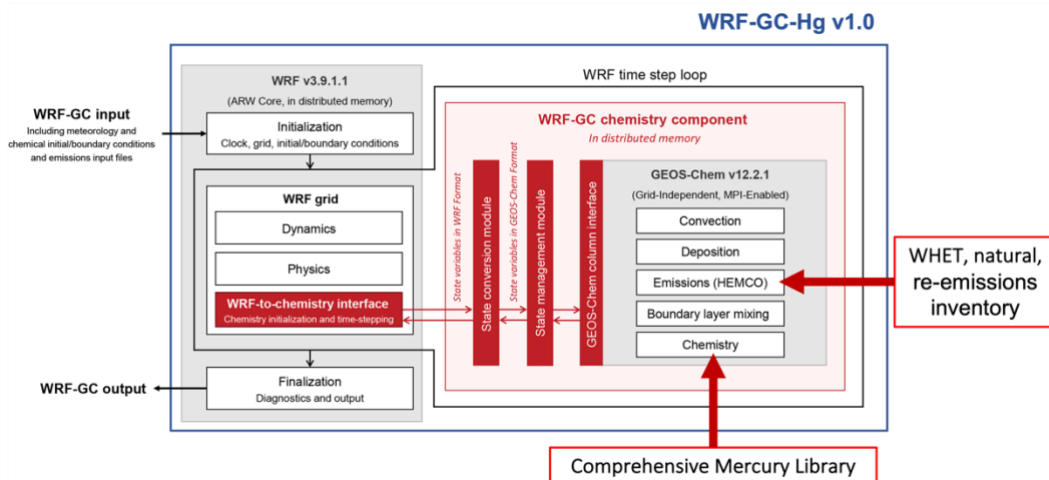
**Fig. 1** WRF-GC-Hg v1.0 framework based on WRF-GC v1.0 (Lin et al., 2020)

105   The WRF-GC model is a regional model that requires initial and lateral boundary conditions, which are provided by a global GEOS-Chem simulation with a consistent setup. In this study, we run the GEOS-Chem Hg simulation at $4° \times 5°$ resolution, driven by GEOS_FP offline meteorological dataset from the Goddard Earth Observation System (GEOS) of NASA Global Modeling and Assimilation Office (GMAO) with 47 vertical layers. The GEOS-Chem simulation is configured to start to run a few days earlier than the WRF-GC simulation. The lateral boundary conditions of other species (e.g., Br and $NO_2$) are also

110   provided by a standard GEOS-Chem full chemistry simulation that is driven by the same resolution and meteorological data as the Hg simulation. The output of the GEOS-Chem Hg and full chemistry simulations are then processed and combined before feeding to the WRF-GC model.
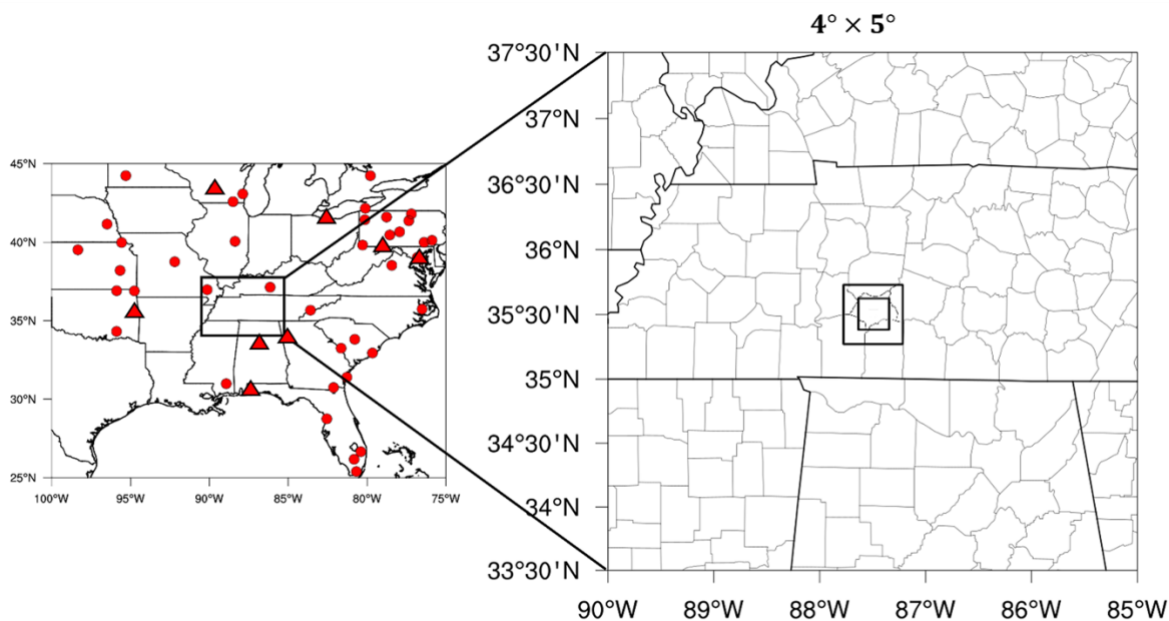
**Fig. 2** Model simulation domain (Left panel: black box represents a single grid of GEOS-Chem 4° × 5° simulation, red circle dots represent MDN sites and triangle dots represents AMNet sites within this domain; Right panel: boxes from outside to inside respectively represents one grid of the resolution of 4° × 5°, 50km × 50km, 25km × 25km)

We set up a simulation domain over the southeastern US and a simulation period of July-September 2013 because convective precipitation is normally concentrated in summer (Holmes et al., 2016; Fulkerson and Nnadi, 2006). The model domain extends west-east from the middle of Texas to Pennsylvania and north-south from the Canadian border to Florida (Fig. 2). We ran simulations with different horizontal resolutions (50 km × 50 km and 25 km × 25 km for WRF-GC and 4° × 5° for GEOS-Chem) rather than using nested domains. These horizontal resolutions result in 106 × 111 grid boxes for a horizontal resolution of 25 km, and 51 × 65 boxes for a resolution of 50 km. Table 1 lists the physical setup and configuration for the WRF model following Feng et al., 2021 and Lin et al., 2020. Large-scale meteorological datasets used for WRF-GC are from National Centers for Environmental Prediction (NCEP) FNL Operational Global Analysis data at 1°× 1° resolution with 6-hour interval (doi:10.5065/D6M043C6). The meteorological data and tracer advection are handled by the WRF model component, while emission, convective transport, chemistry, deposition, and boundary layer mixing are calculated by the GEOS-Chem module. These two model components exchange data online during runtime. This enables WRF-GC Hg simulation to be run at a customized high resolution that stand-alone GEOS-Chem cannot realize. We archive hourly meteorological variables, chemical tracer concentrations, and wet deposition fluxes of $Hg^2$ for analysis.

**Table 1** Physical parameters

| Physics | |
|---|---|
| Microphysics | Morrison Double-Monment scheme (Morrison et al., 2009) |
| Cumulus | New-Tiedtke scheme (M.Tiedtke, 1989) |
| Radiation | RRTMG (both longwave & shortwave) (Iacono et al., 2008) |
| Land Surface | Noah Land Surface Model(Chen and Dudhia, 2001a, b) |
| PBL | Mellor-Yamada Nakanishi Niino scheme (Nakanishi and Niino, 2006) |
| Surface | MM5 Monin-Obukhov (Jiménez et al., 2012) |

Fig. 3 compares the precipitation during July-September 2013 between WRF-GC at different resolutions and CPC Merged Analysis of Precipitation (CMAP) data. The CMAP is $2.5° \times 2.5°$ monthly analyses of global precipitation, generated from merging rain gauges and several satellite-based algorithms (Xie and Arkin, 1997). The average total precipitation of WRF-GC 25km $\times$ 25km is 3.49 mm/day for the whole simulation region during 3 months in 2013, consistent with the CMAP data (3.16 mm/day). The spatial distribution of the WRF-GC model resembles that of the CMAP data, with the highest precipitation in the northern Gulf of Mexico and extending to the nearby continental regions. The average precipitation over the southeast most region (75°W ~ 95°W, 25°N ~ 35°N) is substantially higher (4.63mm/day), which also agrees with the CMAP data (4.51 mm/day). We further divide the total precipitation from WRF-GC simulation to non-convective (or stratiform) and convective parts. The WRF-GC model suggests that convective precipitation accounts for ~90% of total precipitation in this region (Fig. 3).
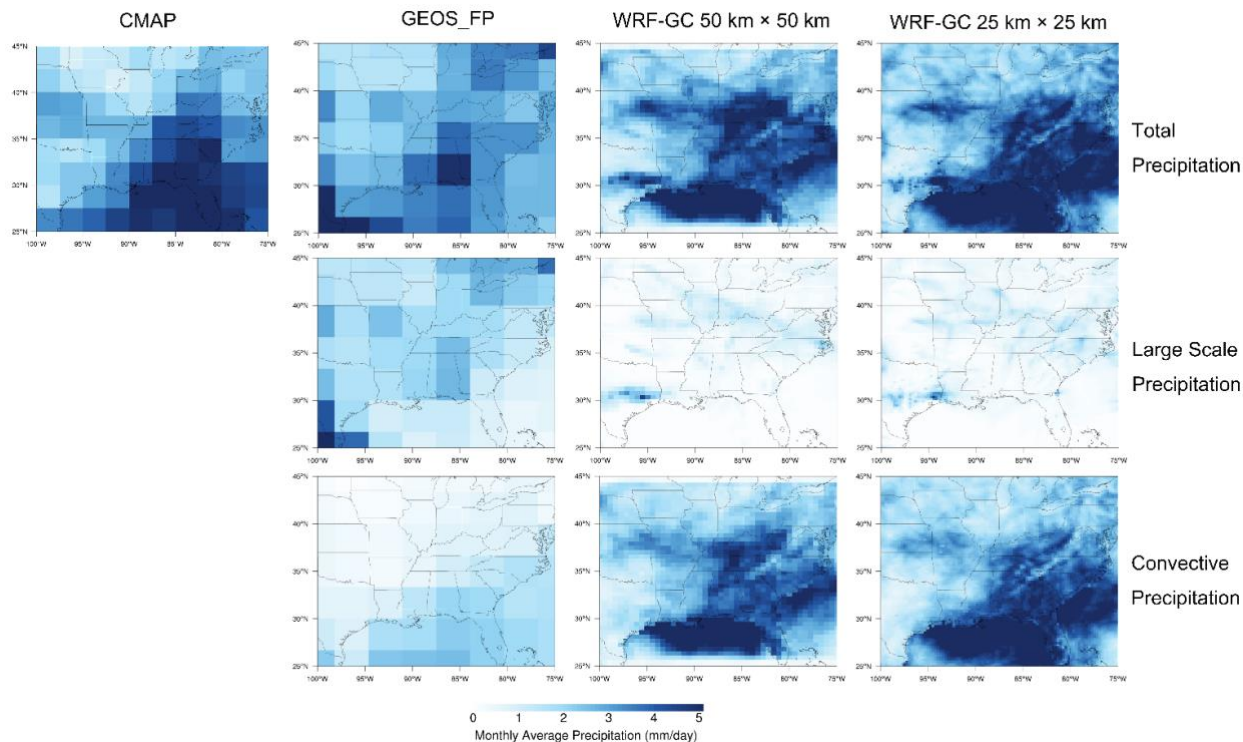
**Fig. 3** Monthly average precipitation from July to September 2013 (Left top corner: CPC Merged Analysis of Precipitation; From the second to fourth column: GEOS_FP offline meteorological dataset, WRF-GC precipitation in 50km × 50km, 25km × 25km resolution; From top to bottom: three-month average precipitation, non-convective precipitation, convective precipitation)

The average total precipitation of WRF-GC 25km × 25km is 3.49 mm/day for the whole simulation region, of which convective precipitation and non-convective precipitation account for 3.11 mm/day and 0.39 mm/day. However, when the simulation narrows down to the southeast-most region (75°W ~ 95°W, 25°N ~ 35°N), the average total precipitation increases to 4.63mm/day and convective precipitation increases to 4.33 mm/day, while the large-scale precipitation decreases to 0.29 mm/day. This shows that although the southeastern region only takes up 1/3 of the whole simulation area, the total precipitation and convective precipitations are 32.66% and 39.23% higher than average, while non-convective is 25.64% lower than the average of the whole simulation domain.

**1.2 Observation data**

The weekly-based Hg wet deposition data over the MDN sites are extracted from National Atmospheric Deposition Program (NADP) website (http://nadp.slh.wisc.edu/datalib/mdn/weekly/). The development of MDN has been introduced in the introduction part. During the period of this simulation, from July to September 2013, there are over eighty sites inside

this domain having data. Besides, many missing values or unqualified values existed in the MDN dataset since it was collected manually. For example, the NE25 site has only three valid data points in three months. Hence it is important to conduct a quality check before using the data. We only take sites that contain at least 75% availability of data for three months (Holmes et al., 2010). After this quality check, only 55 sites are finally chosen for this study. The atmospheric $Hg^0$ data are extracted from Atmospheric Mercury Network (AMNet) by NADP (http://nadp.slh.wisc.edu/data/AMNet/), and eight AMNet sites are chosen (see SI Table S2).

## 3 Results and discussion

### 3.1 Comparison of Mercury Concentration between WRF-GC, GEOS-Chem, and AMNet

We compare the WRF-GC modeled $Hg^0$ concentrations to AMNet observations to evaluate the model performance (Fig. 4). Due to the relatively long residence time of $Hg^0$, the concentration distributions are relatively uniform in the model domain. The average $Hg^0$ concentrations are $1.25\pm0.22$ ng m$^{-3}$ for the eight sites in the southeast US, which agree well with GEOS-Chem results $1.27\pm0.06$ ng m$^{-3}$. WRF-GC ($1.61\pm0.20$ ng m$^{-3}$) model does not agree with the observations or GEOS-Chem relatively well but close. This might be due to the development of WRF-GC (Hg chemistry library) coupling GEOS-Chem full-chemistry library with offline Br simulation. Even though all parameters were set the same as running GEOS-Chem, aqueous reductions and aerosol concentration may not be the same as GEOS-Chem's results. The WRF-GC model simulates more elevated $Hg^0$ concentrations in the Ohio River Valley regions than the GEOS-Chem, by which the coarse resolution smoothens out the higher anthropogenic emissions from mainly utility coal burning (Zhang et al., 2012). Similar patterns are simulated for $Hg^2$ and HgP by WRF-GC due to their shorter residence time in the atmosphere. The influence of large point sources on nearby regions is even more distinct in WRF-GC simulations with higher resolutions. Whereas the GEOS-Chem model cannot capture the hotspots of $Hg^2$ and HgP concentrations associated with point sources largely limited by its resolution. However, both models show substantially higher near-surface $Hg^2$ (GEOS-Chem: $5.98\pm1.94$ pg m$^{-3}$, WRF-GC: $13.2\pm7.74$ pg m$^{-3}$, vs AMNet: $3.56\pm6.09$ pg m$^{-3}$). HgP of WRF-GC ($3.32\pm2.34$ pg m$^{-3}$) is similar to AMNet: $3.48\pm2.02$ pg m$^{-3}$ and largely higher than GEOS-Chem ($0.57\pm0.42$ ng m$^{-3}$). This is likely caused by the potential low sampling bias of the annular denuder coating with potassium chloride (KCl) method(McClure et al., 2014; Lyman et al., 2010; Gustin et al., 2015) used by AMNet $Hg^2$/HgP measurements, Zhang et al., 2012 compared to the concurrent side-by-side cation exchange membrane measurements (Lyman et al., 2020). Another possible reason is various sampling efficiency under conditions of higher atmospheric ambient ozone and high-level relative humidity caused uncertainties for GOM (Gustin et al., 2013, 2015; Weiss-Penzias et al., 2015; Huang and Gustin, 2015).
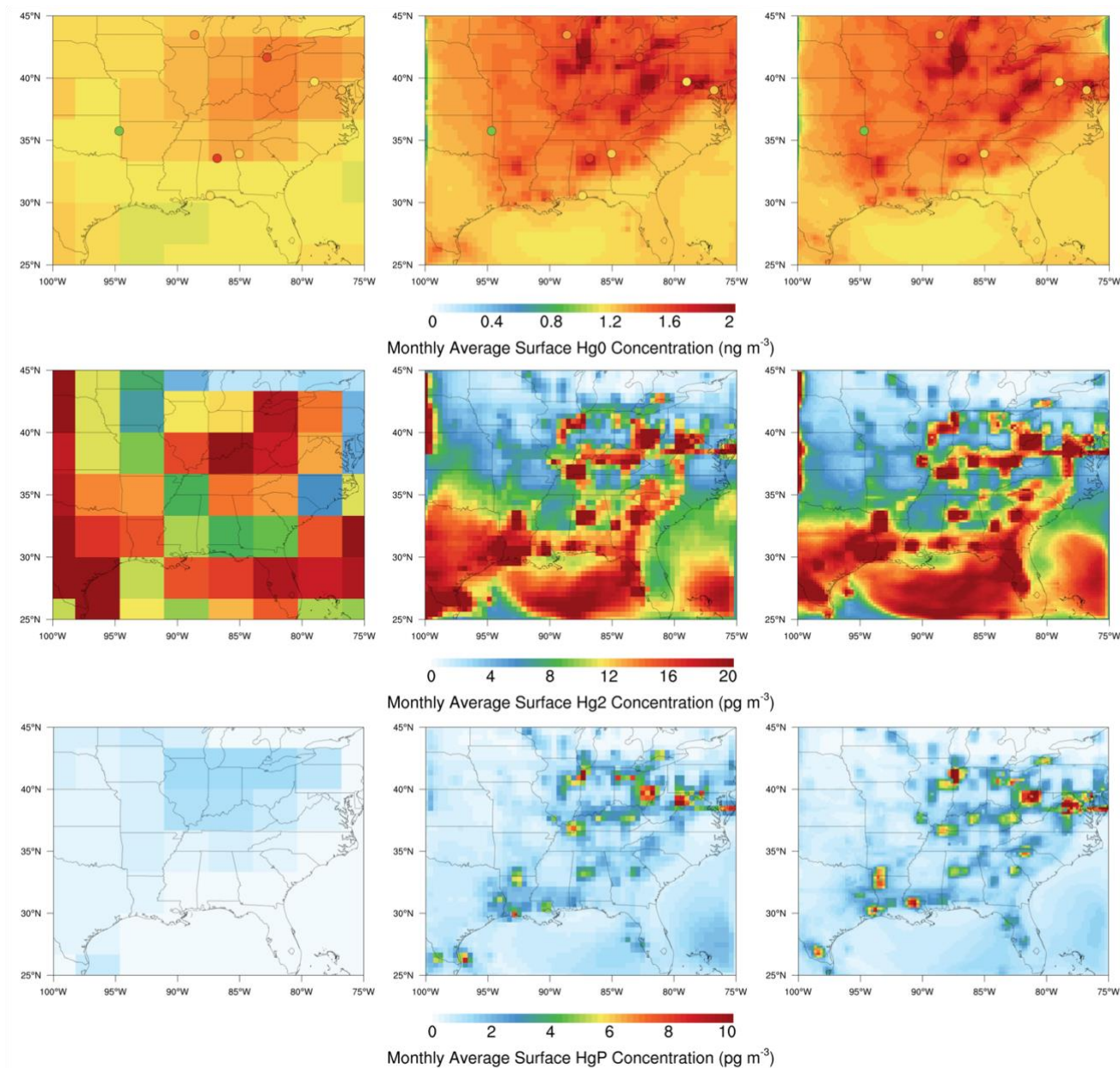
**Fig. 4** Comparison of monthly average Hg surface concentration of $Hg^0$ (top), $Hg^2$ (middle), HgP (bottom) from July to September 2013. The left panel is GEOS-Chem $4° \times 5°$ simulation. The other two columns from left to right correspond to different WFF-GC resolutions: 50 km $\times$ 50 km, 25 km $\times$ 25 km. Dots on the top row of the panel represents $Hg^0$ observation data from AMNet of NADP (http://nadp.slh.wisc.edu/AMNet/).

## 3.2 Comparison of Hg Wet Deposition between WRF-GC, GEOS-Chem, and MDN

195    Fig. 5 shows the modeled Hg wet deposition fluxes in the southeast US during July-September 2013, compared to MDN observations. We include the $Hg^2$ and HgP wet deposition caused by both large-scale (LS or non-convective) and convective (CONV) precipitations. The GEOS-Chem model is included as a benchmark while the WRF-GC at different spatial resolutions (from 50 km to 25 km) are also shown. The MDN sites observed an average of 3.27±1.90 µg m$^{-2}$ for all the 55 sites of the domain in the three months. There is a clear spatial pattern for the flux with higher deposition (6.25±1.48

200 µg m$^{-2}$) over the 12 sites in southeast-most of the US (in Georgia, Alabama, Mississippi, South Carolina, and Florida states) than the other 43 sites (2.44±0.93 µg m$^{-2}$). Both the GEOS-Chem and WRF-GC simulate similar Hg wet deposition patterns with the observations: 0 to 3 µg m$^{-2}$ in the top-left part of the simulation domain, > 4 µg m$^{-2}$ in areas close to the Gulf of Mexico area. However, we find a significant underestimation for these 12 sites by the GEOS-Chem model (3.33 µg m$^{-2}$, 46% lower than MDN). With higher resolutions, the modeled values increase to 2.86±1.07 µg m$^{-2}$ (50 km), 4.16±1.21 µg m$^{-2}$ (25

205 km), which gradually fix the underestimation as the resolution increase.
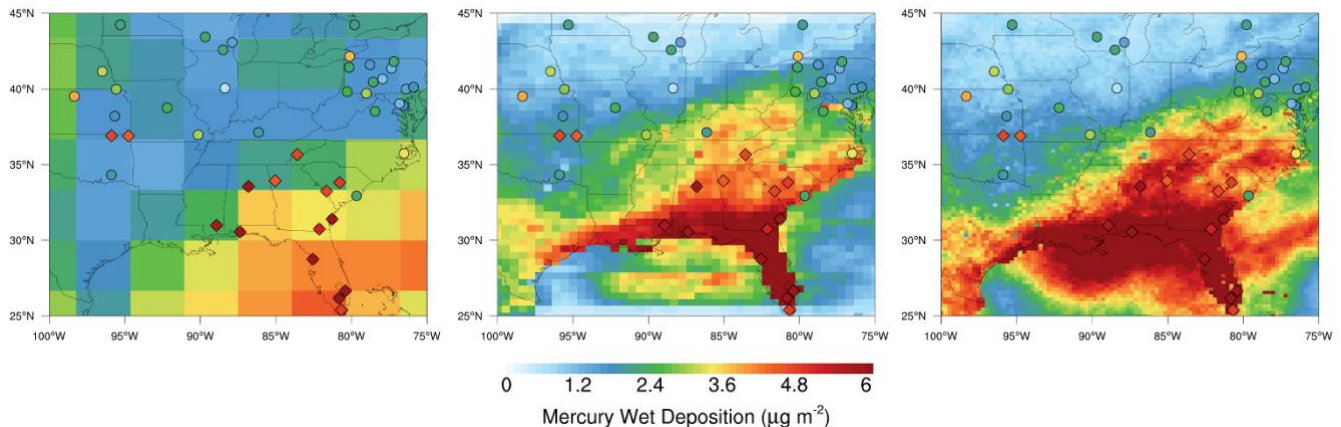
**Fig. 5** Comparison of total Hg Wet Deposition by different model simulations from July to September 2013. The left panel is GEOS-Chem 4° × 5° simulation. The other two columns from left to right correspond to different WFF-GC resolutions: 50 km × 50 km, 25 km × 25 km. The dots in the circle represents wet deposition lower than 4 µg m$^{-2}$ and dots in rhombus

210 represent higher than 4 µg m$^{-2}$.

## 3.3 Week-to-week Comparison of Hg Wet Deposition between WRF-GC, GEOS-Chem, and MDN

    The MDN sites collect weekly precipitation samples and an ideally total of ~12 samples are included in the three-month period we studied. Fig. 6 compares the measured weekly Hg wet deposition flux over the 12 sites with higher values with the GEOS-Chem and WRF-GC models with different resolutions (plots for the other sites are shown in Fig. S4). The

215 highest deposition fluxes. For example, the FL05 site at Florida state has a total deposition flux of 9.19 µg m$^{-2}$ in the three

months, while the largest three weeks (6-27/Aug) contribute 57% with the other 9 weeks contributing only 43%. Similar patterns are also observed in FL34, FL11, MS22, GA40, and SC19.
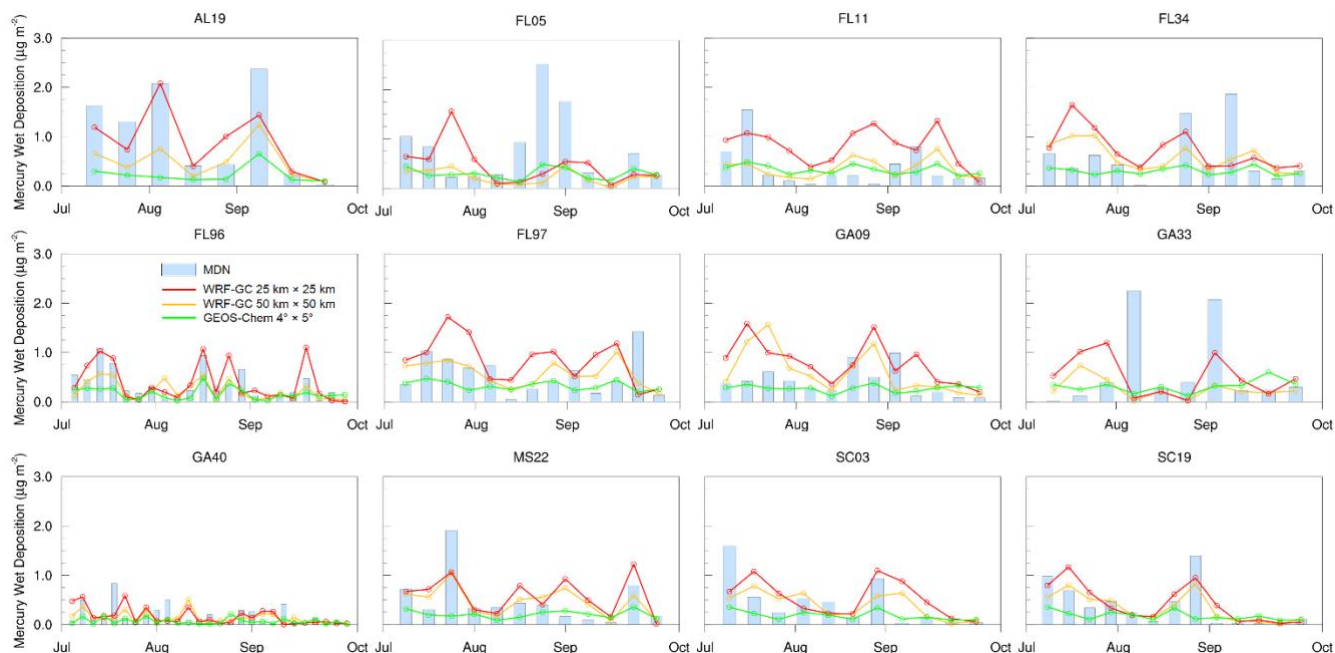
**Fig. 6** Time series plot of comparison of MDN observation, GEOS-Chem 4° × 5° and WRF-GC 50 km × 50 km, 25 km × 25 km simulation results. This plot only shows MDN sites in Florida, full-time series plots in SI.

Therefore, we assume that the reason for the underestimation of Hg wet deposition in GEOS-Chem is the loss of peak value. For example, the second sampling period of FL11 in Fig. 6, where MDN captures 1.54 µg m$^{-2}$, both GEOS-Chem 4° × 5° and WRF-GC 50 km × 50 km simulated a value of 0.48 µg m$^{-2}$, while WRF-GC 25 km × 25 km shows a value of 0.98 µg m$^{-2}$. As the resolution increases, WRF-GC can better grasp the convective precipitation on a small scale than the GEOS-Chem simulation. However, we find that this increase of resolution is finite because the improvement of the increase of wet deposition flux is not that obvious as WRF-GC resolution increases. Fig. 7 shows analysis of four short-period cases for 12 high-value MDN sites in July (week 1: 2-9; week 2: 10-16; week 3: 17-23; week 4: 24-30). From GEOS-Chem 4° × 5° to WRF-GC 50 km × 50 km (~0.5°), though GEOS-Chem has a better correlation coefficient for most of the time, the slope of high-resolution simulation of WRF-GC is much closer to 1:1 line than GEOS-Chem simulation. This result also proves the underestimation of GEOS-Chem simulation in Hg wet deposition. As the WRF-GC resolution increases to 25 km × 25 km (~0.25°), the results are higher than the results from 50 km × 50 km resolution. Here the increase of resolution is only better for meteorology simulation because finer resolution can help the model resolve small-scale weather conditions. Since the resolution of emission inventories is fixed (1° × 1° and 4° × 5°), with higher resolution, more Hg wet deposition will be shown in our result because more convective precipitation captured by the model.
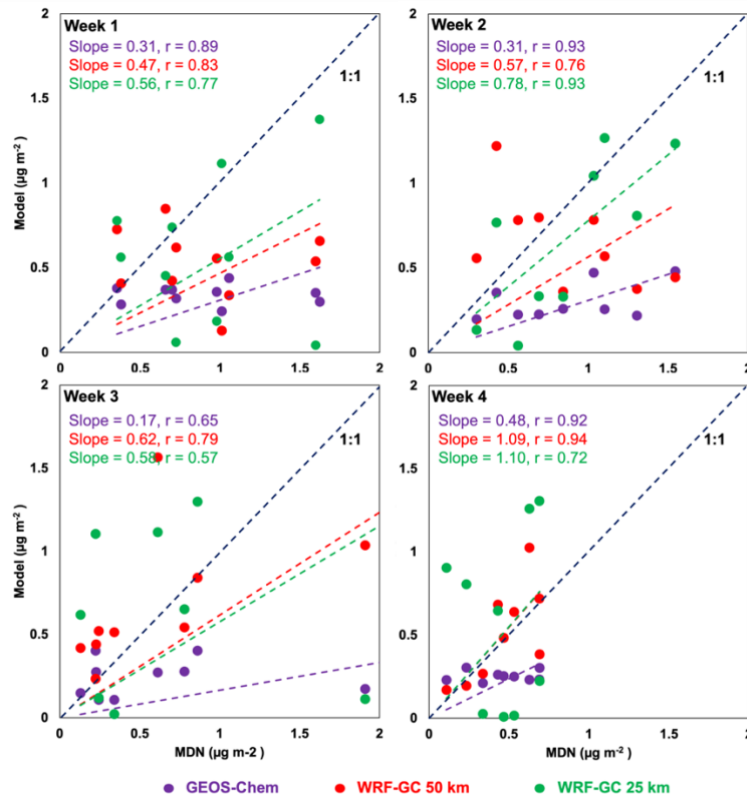
235

**Fig. 7** Comparison of correlation analysis of different simulations for four separate weeks in 12 high-value MDN sites.

### 3.4 Comparison of Vertical Structure of Hg Wet Deposition between WRF-GC and GEOS-Chem

Fig. 8 shows the vertical structure of total Hg wet deposition simulated by the GEOS-Chem and WRF-GC models. Both GEOS-Chem and WRF-GC present a rising (4km) trend first and falling (8km), with the highest occurring at ~6km. Hg wet deposition only exists in the border of the Gulf of Mexico and Florida and each model shows Florida has the highest value (GEOS-Chem; 0.2 $\mu$g m$^{-2}$, WRF-GC: 0.4 $\mu$g m$^{-2}$) at this level. At the height increase to ~6 km, the distribution of Hg wet deposition becomes larger with the value of ~0.4 $\mu$g m$^{-2}$ for two models and more places have Hg wet deposition larger than 0.4 $\mu$g m$^{-2}$. When the height increases to ~8 km, Hg wet deposition in other regions starts to fall, and only southeast-most areas still present higher value. Although GEOS-Chem 4° × 5° simulation has some differences with WRF-GC 50 km × 50 km and 25 km × 25 km simulation, the whole trend and distribution are similar. Therefore, to better understand which specific type of precipitation caused high Hg wet deposition, we divided the total Hg wet deposition into two types: large-scale-caused Hg wet deposition (LS or non-convective) and convective-caused Hg wet deposition (CONV).
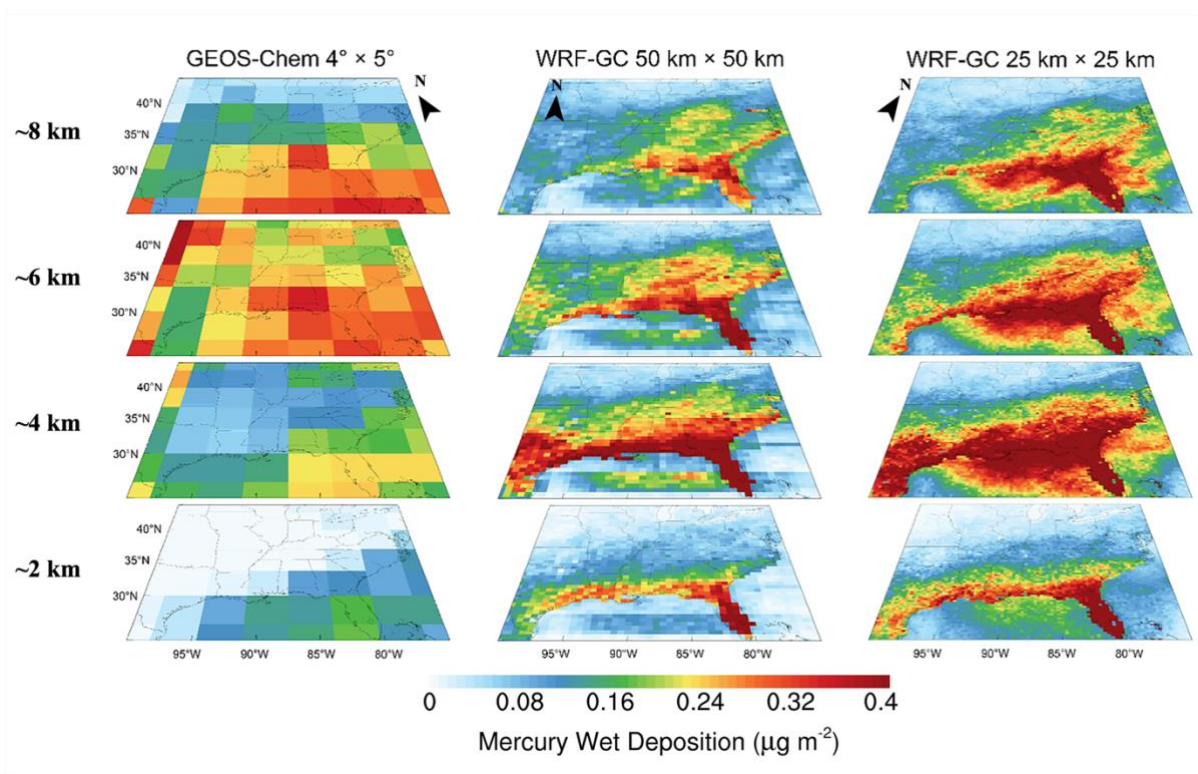
**Fig. 8** Comparison of total Hg wet deposition of GEOS-Chem and WRF-GC at different levels and resolution. From top to bottom is the simulation results for ~2 km, ~4 km, ~6 km, ~8 km level, respectively. The first column is GEOS-Chem 4° × 5° simulation results. The other two from left to right correspond to different WFF-GC resolutions: 50 km × 50 km, 25 km × 25 km.

## 3.5 Comparison of Different Type of Hg Wet Deposition between WRF-GC and GEOS-Chem

The first and second rows of Fig. 9 show Hg wet deposition caused by LS and CONV, respectively. LS of GEOS-Chem is slightly higher than that of WRF-GC, but we can still clearly see the higher value of > 2 µg m$^{-2}$ distributed in the southeast-most area. However, for CONV, although two models share higher Hg wet deposition in the same area, CONV of GEOS-Chem is lower than 1.8 µg m$^{-2}$, where CONV of WRF-GC is normally higher than 3 µg m$^{-2}$. Besides, we calculated the percentage of LS, CONV, and ratio of LS/CONV from a different model, respectively. CONV in GEOS-Chem only takes 23.41% of total Hg wet deposition in this domain, while WRF-GC has 61.54% of Hg wet deposition resulting from CONV. The ratio of LS/CONV of GEOS-Chem is 3.27 and of WRF-GC is 0.56. These both preliminarily verified that Hg wet deposition in the southeastern US came from convective precipitation. To further prove the height of convective precipitation that caused high Hg wet deposition, we divided these two types of Hg wet deposition by height.
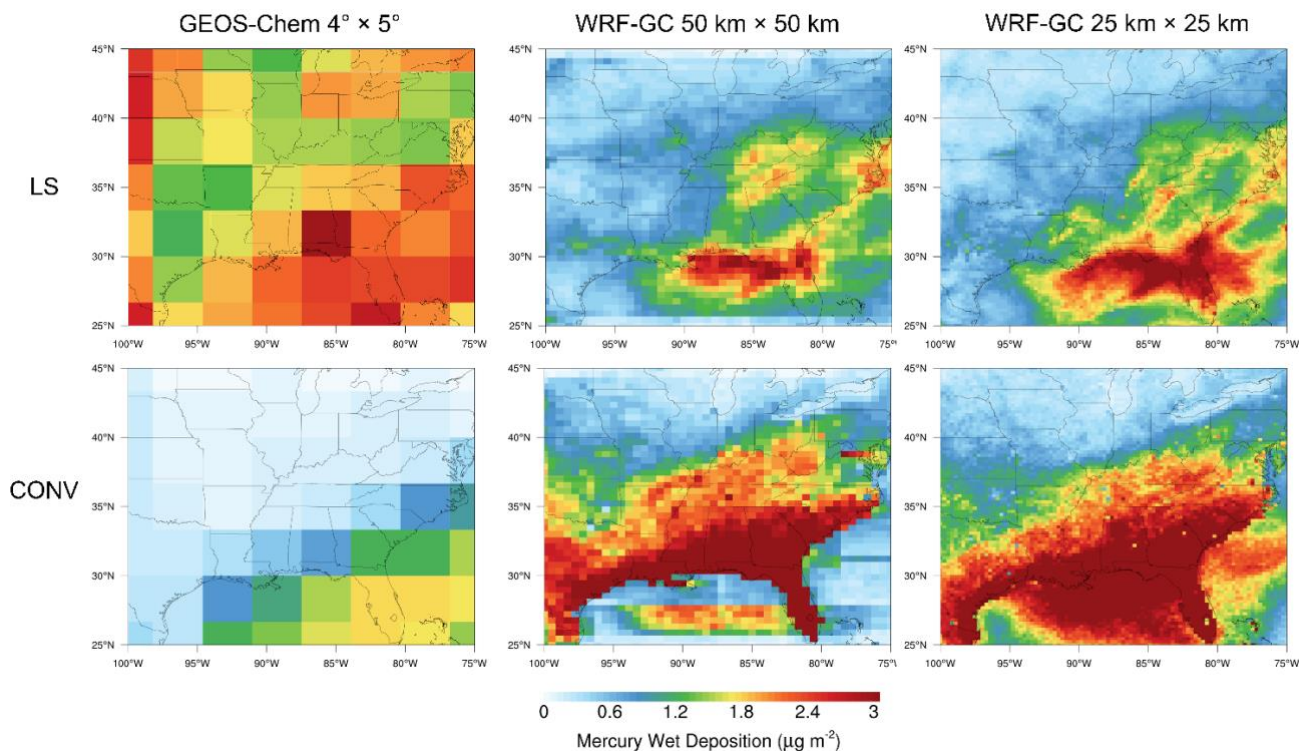
**Fig. 9** Comparison of different types of wet deposition of GEOS-Chem and WRF-GC. The top panel shows LS, and the bottom panel shows CONV. The first column is GEOS-Chem $4° \times 5°$ simulation results. Other columns from left to right correspond to different WFF-GC resolutions: 50 km $\times$ 50 km, 25 km $\times$ 25 km.

## 3.6 Comparison of Vertical Structure for Different Type of Hg Wet Deposition between WRF-GC and GEOS-Chem

Fig. 10 shows Hg wet deposition by LS from GEOS-Chem and WRF-GC at different resolutions and heights. LS from GEOS-Chem and WRF-GC both increases as the height increase and the two models all have value $< 0.1\mu g\ m^{-2}$ under ~6km. However, LS from GEOS-Chem is much larger than WRF-GC at a height of ~6 km, we assume this might be caused by the GEOS_FP meteorological data because large-scale precipitation is stronger than WRF-GC in Fig. 2. LS at ~8 km is the same for the two models, but as the resolution increase, the description of the distribution of the Hg wet position is getting better. Fig. 11 shows Hg wet deposition by CONV from GEOS-Chem and WRF-GC at different resolutions and heights. We can see the higher CONV of the two models both distributed in the southeast-most area and presents an increasing trend until ~4 km and decrease later. CONV of GEOS-Chem is all lower than 0.15 $\mu g\ m^{-2}$ but WRF-GC can reach 0.8 $\mu g\ m^{-2}$ at ~4 km, 0.5 $\mu g\ m^{-2}$ at ~6 km and remain 0.3 $\mu g\ m^{-2}$ at ~8 km. Besides, by comparing the different resolutions of WRF-GC simulation, the distribution of Hg wet deposition is getting more and more continuous. Also, because higher

resolution can capture the peak Hg wet deposition by convective precipitation in a small domain, the total Hg wet deposition slightly increases with the resolution.
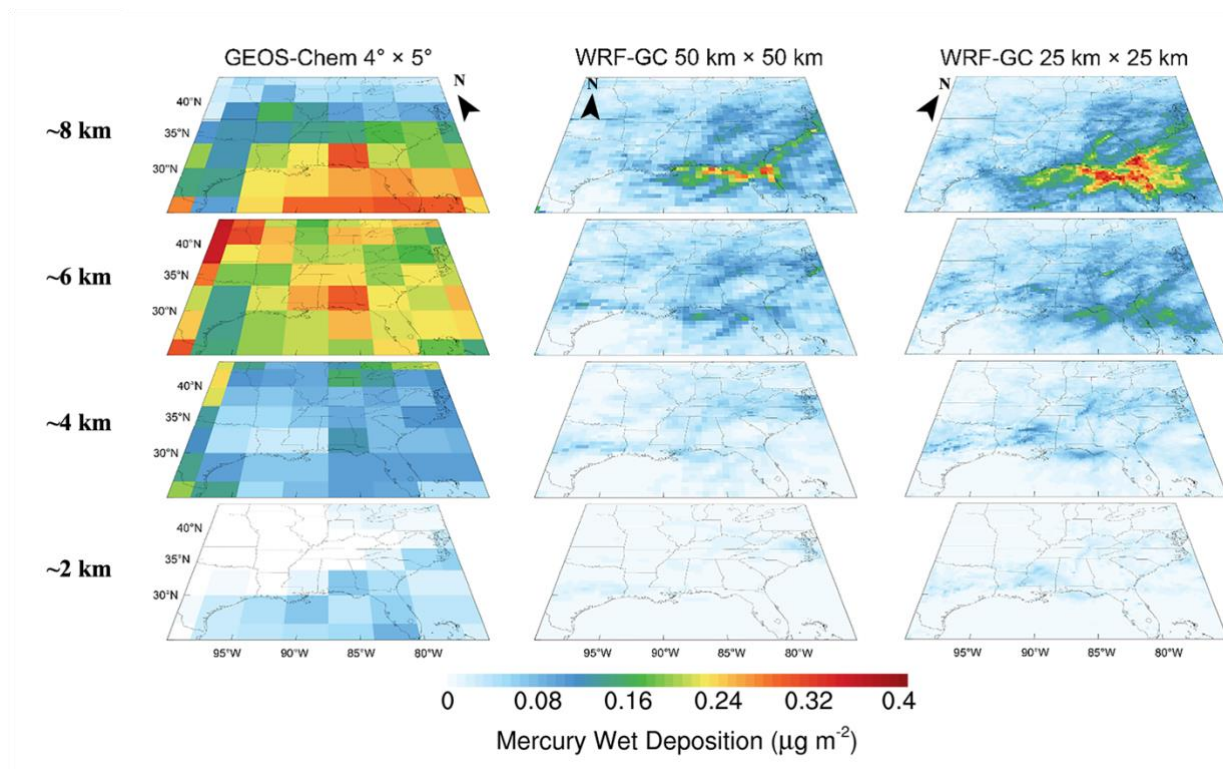
280

**Fig. 10** Comparison of LS of GEOS-Chem and WRF-GC at different levels and resolutions. From top to bottom stands for Hg wet deposition at ~2 km, ~4 km, ~6 km, ~8 km, respectively. The first column is GEOS-Chem $4° \times 5°$ simulation results. Other columns from left to right correspond to different WFF-GC resolutions: 50 km $\times$ 50 km, 25 km $\times$ 25 km.
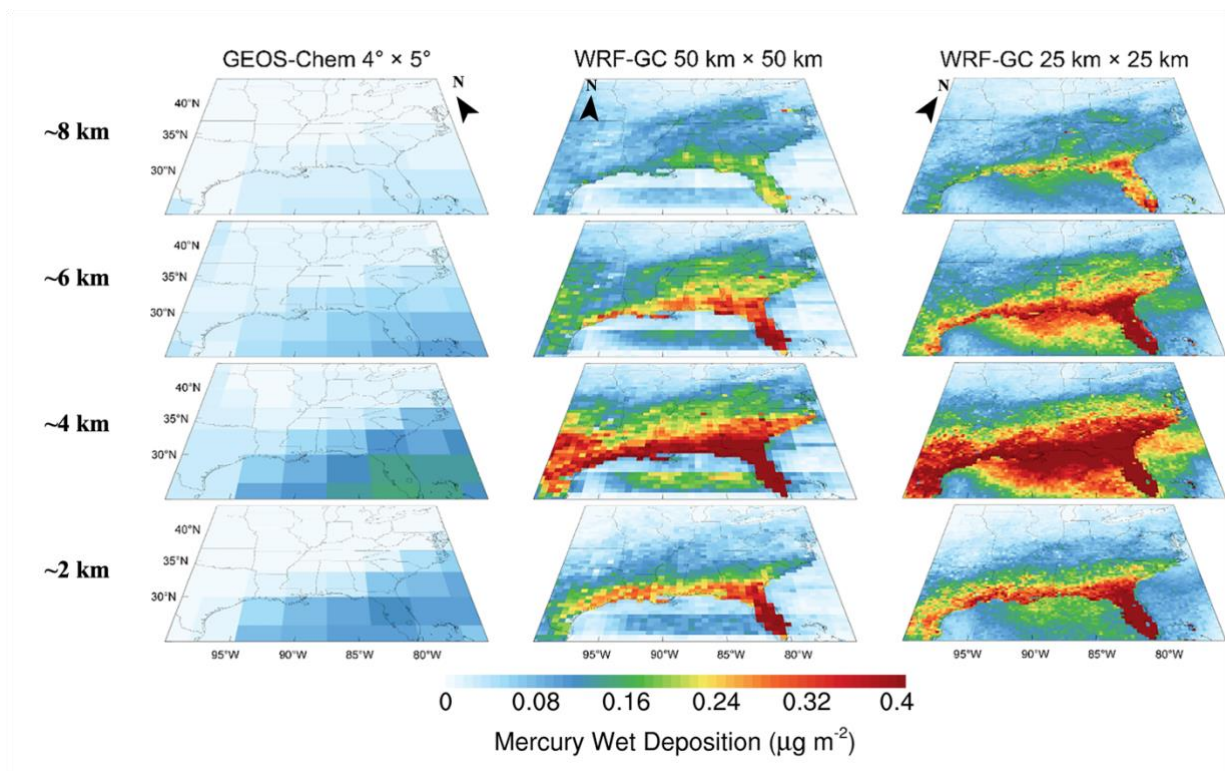
Fig. 11 Comparison of CONV of GEOS-Chem and WRF-GC at different levels and resolutions. From top to bottom stands for Hg wet deposition at ~2 km, ~4 km, ~6 km, ~8 km, respectively. The first column is GEOS-Chem $4° \times 5°$ simulation results. Other columns from left to right correspond to different WFF-GC resolutions: 50 km $\times$ 50 km, 25 km $\times$ 25 km.

**Conclusion**

This study applies a new coupled WRF-GC v1.0 model and develops comprehensive codes of Hg simulation into the model (WRF-GC-Hg v1.0) to explain the reason for higher wet deposition in the southeastern United States. Boundary conditions are provided by a global GEOS-Chem Hg simulation at $4° \times 5°$ resolution with the same emissions and chemistry. Comparisons between WRF-GC simulation in 50km $\times$ 50km, 25km $\times$ 25km resolution, GEOS-Chem Hg simulation results at $4° \times 5°$ resolution, and observation dataset from AMNet and MDN were extensively conducted. WRF-GC simulated an average $Hg^0$ concentration of $1.61\pm0.20$ ng m$^{-3}$, which agrees with GEOS-Chem simulation $1.27\pm0.06$ ng m$^{-3}$ and AMNet observation $1.25\pm0.22$ ng m$^{-3}$. There is a large difference of $Hg^2$/HgP concentration from AMNet to two models, which we suggest is caused by the potential low sampling bias of the traditional annular denuder coating with potassium chloride method used by AMNet $Hg^2$/HgP measurements.

Regarding Hg wet deposition, two models have a similar distribution in the southeast-most area, but the value of Hg wet deposition of WRF-GC ($3.48\pm2.02$ µg m$^{-2}$) is closer to MDN sites ($3.27\pm1.90$ µg m$^{-2}$) than GEOS-Chem ($1.25\pm0.22$ µg m$^{-2}$). 12 sites were chosen in the southeast-most area (states of Mississippi, Alabama, Georgia, South Carolina, and Florida) since higher values usually happen in this region. After analyzing time-series variation, we found that Hg wet deposition came from a few short periods but was not evenly distributed in three months, which corresponds to the occurrence of convective precipitation.

To prove the higher Hg wet deposition came from convective precipitation at higher space. We first describe Hg wet deposition with a different model at a different height. It is clear that Hg wet deposition from two models increases with height first and then decreases, and most of Hg wet deposition was at a higher height. Then we divided Hg wet deposition by different types of precipitation: large-scale and convective. LS of GEOS-Chem is slightly higher than that of WRF-GC, but we can still clearly see the higher value of $> 2$ µg m$^{-2}$ in the southeast-most area. However, CONV of GEOS-Chem is lower than 1.8 µg m$^{-2}$ while that of WRF-GC is normally higher than 3 µg m$^{-2}$. Besides, the ratio of LS/CONV from GEOS-Chem is 3.27 and of WRF-GC is 0.56 since CONV in GEOS-Chem only takes 23.41% of total Hg wet deposition in this domain, while WRF-GC has 61.54% of Hg wet deposition. At last, we combine the two abovementioned analyses and elaborate Hg wet deposition by different types of precipitation at different heights. LS from GEOS-Chem and WRF-GC both increases as the height increase and the two models all have value $< 0.1$µg m$^{-2}$ under ~6km, whilst LS from GEOS-Chem is much larger than WRF-GC at a height of ~6 km, we assume GEOS_FP meteorological data might cause this situation. CONV from GEOS-Chem and WRF-GC are both distributed in the southeast-most area and present an increasing trend until ~4 km and decrease later. However, CONV of GEOS-Chem is all lower than 0.15 µg m$^{-2}$ whilst WRF-GC can reach 0.8 µg m$^{-2}$ at ~4 km, 0.5 µg m$^{-2}$ at ~6 km and remain 0.3 µg m$^{-2}$ at ~8 km. This may slightly be different from previous research in that high Hg wet deposition was scavenged by a supercell thunderstorm at a height of over 10 km.

In addition, by comparing the different resolutions of WRF-GC simulation, the distribution of Hg wet deposition is getting more and more continuous. Also, because higher resolution can grasp the peak Hg wet deposition by convective precipitation in a small domain, the total Hg wet deposition slightly increases with the resolution. However, we need to notice that the increase of simulation performance with an increase of resolution is finite.

*Code availability*

The parent WRF-GC v1.0 model is open source and can be accessed at http://wrf.geos-chem.org or downloaded from GitHub (https://github.com/jimmielin/wrf-gc-release/tree/v0.9). The code used for implementing mercury into WRF-GC (WRF-GC-Hg v1.0) in this paper can be obtained from GitHub (https://github.com/Jim-Xu/WRF-GC-Hg). The latest WRF-GC-Hg v1.0 is permanently archived at https://doi.org/10.5281/zenodo.6366777 (last access: 18th Mar 2022).

*Author contribution*

YZ supervised and guided the whole project, XX did all simulations, analysis, and paper writing, XF, HL & TMF provides
330 ample technical advice during the code development, PZ & SH & ZS  and YP provides advice and assistance in analyzing
results.

*Competing interests*

The authors declare no competing interest.

335

340

345

350

## References

Ariya, P. A., Amyot, M., Dastoor, A., Deeds, D., Feinberg, A., Kos, G., Poulain, A., Ryjkov, A., Semeniuk, K., Subir, M., and Toyota, K.: Mercury Physicochemical and Biogeochemical Transformation in the Atmosphere and at Atmospheric Interfaces: A Review and Future Directions, 115, 3760–3802, https://doi.org/10.1021/cr500667e, 2015.

Brisson, E., Van Weverberg, K., Demuzere, M., Devis, A., Saeed, S., Stengel, M., and van Lipzig, N. P. M.: How well can a convection-permitting climate model reproduce decadal statistics of precipitation, temperature and cloud characteristics?, 47, 3043–3061, https://doi.org/10.1007/s00382-016-3012-z, 2016.

Bullock, O. R. and Brehme, K. A.: Atmospheric mercury simulation using the CMAQ model: formulation description and analysis of wet deposition results, Atmospheric Environment, 2135–2146 pp., 2002.

Chen, F. and Dudhia, J.: Coupling an advanced land surface-hydrology model with the Penn-State-NCAR MM5 modeling system. Part II: Preliminary model validation, 129, 587–604, https://doi.org/10.1175/1520-0493(2001)129<0587:CAALSH>2.0.CO;2, 2001a.

Chen, F. and Dudhia, J.: Coupling and advanced land surface-hydrology model with the Penn State-NCAR MM5 modeling system. Part I: Model implementation and sensitivity, 129, 569–585, https://doi.org/10.1175/1520-0493(2001)129<0569:CAALSH>2.0.CO;2, 2001b.

Coburn, S., Dix, B., Edgerton, E., D Holmes, C., Kinnison, D., Liang, Q., Ter Schure, A., Wang, S., and Volkamer, R.: Mercury oxidation from bromine chemistry in the free troposphere over the southeastern US, 16, 3743–3760, https://doi.org/10.5194/acp-16-3743-2016, 2016.

Damian, V., Sandu, A., Damian, M., Potra, F., and Carmichael, G. R.: The kinetic preprocessor KPP - A software environment for solving chemical kinetics, 26, 1567–1579, https://doi.org/10.1016/S0098-1354(02)00128-X, 2002.

Eastham, S. D., Weisenstein, D. K., and Barrett, S. R. H.: Development and evaluation of the unified tropospheric-stratospheric chemistry extension (UCX) for the global chemistry-transport model GEOS-Chem, 89, 52–63, https://doi.org/10.1016/j.atmosenv.2014.02.001, 2014.

Eastham, S. D., Long, M. S., Keller, C. A., Lundgren, E., Yantosca, R. M., Zhuang, J., Li, C., Lee, C. J., Yannetti, M., Auer, B. M., Clune, T. L., Kouatchou, J., Putman, W. M., Thompson, M. A., Trayanov, A. L., Molod, A. M., Martin, R. V., and Jacob, D. J.: GEOS-Chem high performance (GCHP v11-02c): A next-generation implementation of the GEOS-Chem chemical transport model for massively parallel applications, 11, 2941–2953, https://doi.org/10.5194/gmd-11-2941-2018, 2018.

Feng, X., Lin, H., Fu, T.-M., Sulprizio, M. P., Zhuang, J., Jacob, D. J., Tian, H., Ma, Y., Zhang, L., Wang, X., Chen, Q., and Han, Z.: WRF-GC (v2.0): online two-way coupling of WRF (v3.9.1.1) and GEOS-Chem (v12.7.2) for modeling regional atmospheric chemistry–meteorology interactions, 14, 3741–3768, https://doi.org/10.5194/gmd-14-3741-2021, 2021.

Fu, X., Yang, X., Lang, X., Zhou, J., Zhang, H., Yu, B., Yan, H., Lin, C. J., and Feng, X.: Atmospheric wet and litterfall mercury deposition at urban and rural sites in China, 16, 11547–11562, https://doi.org/10.5194/acp-16-11547-2016, 2016.

Fulkerson, M. and Nnadi, F. N.: Predicting mercury wet deposition in Florida: A simple approach, 40, 3962–3968, https://doi.org/10.1016/j.atmosenv.2006.02.028, 2006.

Gencarelli, C. N., de Simone, F., Hedgecock, I. M., Sprovieri, F., and Pirrone, N.: Development and application of a regional-scale atmospheric mercury model based on WRF/Chem: A Mediterranean area investigation, 21, 4095–4109,

390    https://doi.org/10.1007/s11356-013-2162-3, 2014.

Gonzalez-Raymat, H., Liu, G., Liriano, C., Li, Y., Yin, Y., Shi, J., Jiang, G., and Cai, Y.: Elemental mercury: Its unique properties affect its behavior and fate in the environment, 229, 69–86, https://doi.org/10.1016/j.envpol.2017.04.101, 2017.

Guentzel, J. L., Landing, W. M., Gill, G. A., and Pollman, C. D.: Processes influencing rainfall deposition of mercury in Florida, 35, 863–873, https://doi.org/10.1021/es001523+, 2001.

395    Gustin, M. S., Huang, J., Miller, M. B., Peterson, C., Jaffe, D. A., Ambrose, J., Finley, B. D., Lyman, S. N., Call, K., Talbot, R., Feddersen, D., Mao, H., and Lindberg, S. E.: Do we understand what the mercury speciation instruments are actually measuring? Results of RAMIX, 47, 7295–7306, https://doi.org/10.1021/es3039104, 2013.

Gustin, M. S., Amos, H. M., Huang, J., Miller, M. B., and Heidecorn, K.: Measuring and modeling mercury in the atmosphere: A critical review, 15, 5697–5713, https://doi.org/10.5194/acp-15-5697-2015, 2015a.

400    Gustin, M. S., Amos, H. M., Huang, J., Miller, M. B., and Heidecorn, K.: Successes and challenges of measuring and modeling atmospheric mercury at the part per quadrillion level: a critical review, 3777–3821 pp., https://doi.org/10.5194/acpd-15-3777-2015, 2015b.

Holmes, C. D., Jacob, D. J., Corbitt, E. S., Mao, J., Yang, X., Talbot, R., and Slemr, F.: Global atmospheric model for mercury including oxidation by bromine atoms, 10, 12037–12057, https://doi.org/10.5194/acp-10-12037-2010, 2010.

405    Holmes, C. D., Krishnamurthy, N. P., Caffrey, J. M., Landing, W. M., Edgerton, E. S., Knapp, K. R., and Nair, U. S.: Thunderstorms increase mercury wet deposition, 50, 9343–9350, https://doi.org/10.1021/acs.est.6b02586, 2016.

Horowitz, H. M., Jacob, D. J., Zhang, Y., DIbble, T. S., Slemr, F., Amos, H. M., Schmidt, J. A., Corbitt, E. S., Marais, E. A., and Sunderland, E. M.: A new mechanism for atmospheric mercury redox chemistry: Implications for the global mercury budget, 17, 6353–6371, https://doi.org/10.5194/acp-17-6353-2017, 2017a.

410    Horowitz, H. M., Jacob, D. J., Zhang, Y., DIbble, T. S., Slemr, F., Amos, H. M., Schmidt, J. A., Corbitt, E. S., Marais, E. A., and Sunderland, E. M.: A new mechanism for atmospheric mercury redox chemistry: Implications for the global mercury budget, 17, 6353–6371, https://doi.org/10.5194/acp-17-6353-2017, 2017b.

Huang, J. and Gustin, M. S.: Uncertainties of gaseous oxidized mercury measurements using KCL-coated denuders, cation-exchange membranes, and nylon membranes: Humidity influences, 49, 6102–6108, https://doi.org/10.1021/acs.est.5b00098,

415    2015.

Iacono, M. J., Delamere, J. S., Mlawer, E. J., Shephard, M. W., Clough, S. A., and Collins, W. D.: Radiative forcing by long-lived greenhouse gases: Calculations with the AER radiative transfer models, 113, 2–9, https://doi.org/10.1029/2008JD009944, 2008.

Jiménez, P. A., Dudhia, J., González-Rouco, J. F., Navarro, J., Montávez, J. P., and García-Bustamante, E.: A revised scheme for the WRF surface layer formulation, 140, 898–918, https://doi.org/10.1175/MWR-D-11-00056.1, 2012.

Kaulfus, A. S., Nair, U., Holmes, C. D., and Landing, W. M.: Mercury Wet Scavenging and Deposition Differences by Precipitation Type, 51, 2628–2634, https://doi.org/10.1021/acs.est.6b04187, 2017.

Lin, H., Feng, X., Fu, T.-M., Tian, H., Ma, Y., Zhang, L., Jacob, D. J., Yantosca, R. M., Sulprizio, M. P., Lundgren, E. W., Zhuang, J., Zhang, Q., Lu, X., Zhang, L., Shen, L., Guo, J., Eastham, S. D., and Keller, C. A.: WRF-GC (v1.0): online coupling of WRF (v3.9.1.1) and GEOS-Chem (v12.2.1) for regional atmospheric chemistry modeling – Part 1: Description of the one-way model, 13, 3241–3265, https://doi.org/10.5194/gmd-13-3241-2020, 2020.

Lin, H., Jacob, D. J., Lundgren, E. W., Sulprizio, M. P., Keller, C. A., Fritz, T. M., Eastham, S. D., Emmons, L. K., Campbell, P. C., Baker, B., Saylor, R. D., and Montuoro, R.: Harmonized Emissions Component (HEMCO) 3.0 as a versatile emissions component for atmospheric models: application in the GEOS-Chem, NASA GEOS, WRF-GC, CESM2, NOAA GEFS-Aerosol, and NOAA UFS models, 14, 5487–5506, https://doi.org/10.5194/gmd-14-5487-2021, 2021.

Long, M. S., Yantosca, R., Nielsen, J. E., Keller, C. A., Da Silva, A., Sulprizio, M. P., Pawson, S., and Jacob, D. J.: Development of a grid-independent GEOS-Chem chemical transport model (v9-02) as an atmospheric chemistry module for Earth system models, 8, 595–602, https://doi.org/10.5194/gmd-8-595-2015, 2015.

Lyman, S. N. and Jaffe, D. A.: Formation and fate of oxidized mercury in the upper troposphere and lower stratosphere, 5, 114–117, https://doi.org/10.1038/ngeo1353, 2012.

Lyman, S. N., Jaffe, D. A., and Gustin, M. S.: Release of mercury halides from KCl denuders in the presence of ozone, 10, 8197–8204, https://doi.org/10.5194/acp-10-8197-2010, 2010.

Lyman, S. N., Gratz, L. E., Dunham-Cheatham, S. M., Gustin, M. S., and Luippold, A.: Improvements to the Accuracy of Atmospheric Oxidized Mercury Measurements, 54, 13379–13388, https://doi.org/10.1021/acs.est.0c02747, 2020.

Mason, R. P., Lawson, N. M., and Sheu, G. R.: Annual and seasonal trends in mercury deposition in Maryland, 34, 1691–1701, https://doi.org/10.1016/S1352-2310(99)00428-8, 2000.

McClure, C. D., Jaffe, D. A., and Edgerton, E. S.: Evaluation of the KCl denuder method for gaseous oxidized mercury using HgBr2 at an in-service AMNet site, 48, 11437–11444, https://doi.org/10.1021/es502545k, 2014.

Morrison, H., Thompson, G., and Tatarskii, V.: Impact of cloud microphysics on the development of trailing stratiform precipitation in a simulated squall line: Comparison of one- and two-moment schemes, 137, 991–1007, https://doi.org/10.1175/2008MWR2556.1, 2009.

M.Tiedtke: A comprehensive Mass Flux Scheme for Cumulus Parameterization in Large-Scale Models, 117, 1989.

Nakanishi, M. and Niino, H.: An improved Mellor-Yamada Level-3 model: Its numerical stability and application to a regional prediction of advection fog, 119, 397–407, https://doi.org/10.1007/s10546-005-9030-8, 2006.

Pan, L., Lin, C. J., Carmichael, G. R., Streets, D. G., Tang, Y., Woo, J. H., Shetty, S. K., Chu, H. W., Ho, T. C., Friedli, H. R., and Feng, X.: Study of atmospheric mercury budget in East Asia using STEM-Hg modeling system, 408, 3277–3291, https://doi.org/10.1016/j.scitotenv.2010.04.039, 2010.

Prestbo, E. M. and Gay, D. A.: Wet deposition of mercury in the U.S. and Canada, 1996-2005: Results and analysis of the NADP mercury deposition network (MDN), 43, 4223–4233, https://doi.org/10.1016/j.atmosenv.2009.05.028, 2009.

455 Rumbold, D. G., Axelrad, D. M., and Pollman, C. D.: Mercury and the everglades. A synthesis and model for complex ecosystem restoration, 1–273 pp., https://doi.org/10.1007/978-3-030-32057-7, 2019.

Sandu, A. and Sander, R.: Technical note: Simulating chemical systems in Fortran90 and Matlab with the Kinetic PreProcessor KPP-2.1, 6, 187–195, https://doi.org/10.5194/acp-6-187-2006, 2006.

Selin, N. E., Javob, D. J., Park, R. J., Yantosca, R. M., Strode, S., Jaeglé, L., and Jaffe, D.: Chemical cycling and deposition
460 of atmospheric mercury: Global constraints from observations, 112, 1–14, https://doi.org/10.1029/2006JD007450, 2007.

Selin, N. E., Jacob, D. J., Yantosca, R. M., Strode, S., Jaeglé, L., and Sunderland, E. M.: Global 3-D land-ocean-atmosphere model for mercury: Present-day versus preindustrial cycles and anthropogenic enrichment factors for deposition, 22, 1–13, https://doi.org/10.1029/2007GB003040, 2008.

Sexauer Gustin, M., Weiss-Penzias, P. S., and Peterson, C.: Investigating sources of gaseous oxidized mercury in dry
465 deposition at three sites across Florida, USA, 12, 9201–9219, https://doi.org/10.5194/acp-12-9201-2012, 2012.

Skamarock, W. C., Klemp, J. B., Dudhia, J., Gill, D. O., Barker, D. M., Duda, M. G., Huang, X.-Y., Wang, W., and Powers, J. G.: A Description of the Advanced Research WRF Model Version 3, 113, https://doi.org/10.5065/D68S4MVH, 2008.

Weiss-Penzias, P., Amos, H. M., Selin, N. E., Gustin, M. S., Jaffe, D. A., Obrist, D., Sheu, G. R., and Giang, A.: Use of a global model to understand speciated atmospheric mercury observations at five high-elevation sites, 15, 1161–1173,
470 https://doi.org/10.5194/acp-15-1161-2015, 2015.

Xie, P. and Arkin, P. A.: Global Precipitation: A 17-Year Monthly Analysis Based on Gauge Observations, Satellite Estimates, and Numerical Model Outputs, 78, 2539–2558, https://doi.org/10.1175/1520-0477(1997)078<2539:GPAYMA>2.0.CO;2, 1997.

Zhang, Y., Jaeglé, L., van Donkelaar, A., Martin, R. v., Holmes, C. D., Amos, H. M., Wang, Q., Talbot, R., Artz, R., Brooks,
475 S., Luke, W., Holsen, T. M., Felton, D., Miller, E. K., Perry, K. D., Schmeltz, D., Steffen, A., Tordon, R., Weiss-Penzias, P., and Zsolway, R.: Nested-grid simulation of mercury over North America, 12, 6095–6111, https://doi.org/10.5194/acp-12-6095-2012, 2012a.

Zhang, Y., Jaeglé, L., Van Donkelaar, A., Martin, R. V., Holmes, C. D., Amos, H. M., Wang, Q., Talbot, R., Artz, R., Brooks, S., Luke, W., Holsen, T. M., Felton, D., Miller, E. K., Perry, K. D., Schmeltz, D., Steffen, A., Tordon, R., Weiss-
480 Penzias, P., and Zsolway, R.: Nested-grid simulation of mercury over North America, 12, 6095–6111, https://doi.org/10.5194/acp-12-6095-2012, 2012b.

Zhang, Y., Jacob, D. J., Horowitz, H. M., Chen, L., Amos, H. M., Krabbenhoft, D. P., Slemr, F., st. Louis, V. L., and Sunderland, E. M.: Observed decrease in atmospheric mercury explained by global decline in anthropogenic emissions, 113, 526–531, https://doi.org/10.1073/pnas.1516312113, 2016a.

485    Zhang, Y., Jacob, D. J., Horowitz, H. M., Chen, L., Amos, H. M., Krabbenhoft, D. P., Slemr, F., St. Louis, V. L., and Sunderland, E. M.: Observed decrease in atmospheric mercury explained by global decline in anthropogenic emissions, 113, 526–531, https://doi.org/10.1073/pnas.1516312113, 2016b.